Nano Research

Open Access

Research Article

Multifunctional bagasse nanocellulose-based composite films for intelligent packaging and physiology signal monitoring

Qiaoyan Wei[1,2], Liangdong Ye[1], Dacheng Li[1], Yanyou Huang[1], Yuling LV[1], Ruibing Shen[1], Ziwei Li[1], Wenda Zhang[3] ✉, Zuocai Zhang[1] ✉, Yaping Du[4] ✉, and Shaorong Lu[1] ✉

[1] *Key Laboratory of New Processing Technology for Nonferrous Metals and Materials Ministry/Guangxi Key Laboratory of Natural and Biomedical Polymer Materials, School of Material Science and Engineering, Guilin University of Technology, Guilin 541004, China*
[2] *School of Biological and Food Engineering, Guangxi Science & Technology Normal University, Laibin 546199, China*
[3] *Advanced Energy Storage Technology Research Center, Shenzhen Institute of Advanced Technology, Chinese Academy of Sciences, Shenzhen 518055, China*
[4] *Tianjin Key Lab for Rare Earth Materials and Applications, Center for Rare Earth and Inorganic Functional Materials, Smart Sensing Interdisciplinary Science Center, Haihe Laboratory of Sustainable Chemical Transformations, School of Materials Science and Engineering, National Institute for Advanced Materials, Nankai University, Tianjin 300350, China*

Cite this article: *Nano Research*, **2025**, *18*, 94907804. https://doi.org/10.26599/NR.2025.94907804

ABSTRACT: Metabolism, transpiration, and invasion of pathogens during the storage and transportation of fruits can lead to significant waste and even food safety issues. Therefore, real-time, rapid, and accurate non-destructive monitoring of physiological information during the storage of fruits and vegetables to assess fruit freshness is crucial. Herein, we engineered a degradable and multifunctional humidity sensing film for monitoring fruit freshness. The film is fabricated through the co-assembly of bagasse cellulose nanocrystals (CNC), okra polysaccharides (OPs), silver nanowires (Ag NWs), and phytic acid (PA), utilizing dynamic hydrogen and phosphate bonds. This innovative design endows the CNC/OPs/PA/Ag NWs (COPA) composite film with outstanding mechanical properties, water resistance, low water vapor permeability, antibacterial, degradability, and moisture-sensing ability. Notably, the proposed COPA humidity sensor exhibits high linearity (R^2 = 0.994), ultralow hysteresis (1.24%), and 32 days of operational stability across a 35%–98% relative humidity (RH) range, enabling precise freshness monitoring during fruit storage. Significantly, the COPA film prolonged the shelf-life of packaged fruit when compared to conventional PE film packaging. This research establishes a foundational framework for next-generation smart sensors in food quality management and biomedical monitoring applications.

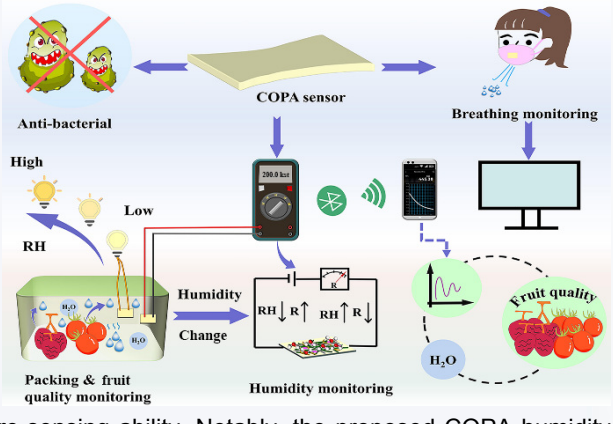

KEYWORDS: high gas barrier, intelligent packaging, physiology signal monitoring, humidity sensor, fruit freshness monitoring

1 Introduction

In recent years, global food security has faced significant pressure due to climate change, frequent extreme weather events, and the impact of the global economy [1]. Fruits and vegetables, heavily relying on their place of origin, often require long-term storage and transportation, during which metabolism, transpiration, and the invasion of pathogenic bacteria can cause a series of problems [2]. On the one hand, they lead to significant food waste, with reports indicating that globally, about one-third of food produced, especially fruits and vegetables, is discarded or wasted annually, accounting for over 40% [3]. On the other hand, consuming fruits contaminated with pathogens poses food safety risks. It is estimated that foodborne illnesses cause over 600 million cases worldwide

Received: April 25, 2025; **Revised:** June 11, 2025
Accepted: July 15, 2025

✉Address correspondence to Shaorong Lu, lushaor@163.com; Zuocai Zhang, zzc12130101@163.com; Wenda Zhang, wd.zhang2@siat.ac.cn; Yaping Du, ypdu@nankai.edu.cn

each year, severely impacting human health and the environment [4]. Therefore, there is an urgent need to develop sensors that can monitor fruit quality information in real time, accurately, and conveniently to address these issues.

Recently, various sensors for monitoring food quality information have been reported. For instance, utilizing a hydrogen-bonded organic framework (Eu@HOF-12), Maimaiti et al. developed a bionic vision-olfactory co-sensory device, which can perform ultrafast, sensitive, and on-site monitoring of biogenic amines (BAs) when combined with a smartphone [5]. Wang et al. developed a pH fluorescent sensor array incorporated with a deep convolutional neural network (DCNN) to achieve accurate classification of vegetable freshness by monitoring alkaline volatile organic compounds (VOCs) in three vegetables: yardlong beans, spinach, and sweet corn [6]. In addition, Du et al. prepared a moisture-sensitive tribo-positive cellulose paper for fruit freshness monitoring using enzymatic digestion [7]. Unfortunately, these sensors are often complicated to manufacture, high cost, lack flexibility, and biodegradability. And they cannot effectively extend the shelf life of packaged foods simultaneously while monitoring freshness.

In fact, the weight loss rate can largely reflect the quality status of fruits and serves as a key index for evaluating the freshness of fruit [8]. The respiration and transpiration processes that occur in harvested fruit result in considerable water loss, which in turn decreases the quality of fruit during storage and transportation. Furthermore, the large amount of water released during fruit spoilage changes the relative humidity of the packaging environment. Therefore, the quality of fruit can be monitored in real time by changes in humidity of packaging microenvironments. Currently, humidity sensors for tracking humidity changes are widely applied in multiple fields, including agricultural and industrial production [9, 10], human-machine interface [11, 12], and human physiological health management [13]. However, to our knowledge, there are fewer reports on the use of flexible humidity sensors for fruit freshness monitoring. Therefore, it is urgent to develop a degradable flexible humidity sensor with excellent antibacterial properties, good mechanical properties, high sensitivity, and long-term stability for fruit preservation and freshness monitoring.

Here, a series of flexible and multifunctional cellulosenanocrystals (CNC)/okra polysaccharides (OPs)/phytic acid (PA)/Ag NWs (COPA) composite films were fabricated using CNC and OPs as the flexible network materials, Ag NWs and PA as the antibacterial and crosslinker, respectively. The permeation mechanism of H_2O molecules through the film was revealed by molecular dynamics simulation (MDS). The optimized COPA film was subsequently functionalized as a core sensing element in a flexible humidity detection platform for real-time fruit freshness assessment. The relationship between fruit quality and the response signal of the COPA humidity sensor, as well as the fruit preservation ability of COPA films on fruits, was investigated, which provided a novel approach to environmental protection and flexible wearable sensors in the field of food preservation and freshness monitoring.

2 Results and discussion

2.1 Design of COPA films

The preparation strategy of COPA films is illustrated in Scheme 1. First, cellulose derived from sugarcane bagasse (SCB) was reacted with chloroacetic acid to produce CNC. Then, CNC and OPs were combined with PA and Ag NWs to fabricate the COPA films. The abundant hydrophilic groups (–OH, –COOH) on CNC and OPs molecular chains impart exceptional humidity sensitivity to the

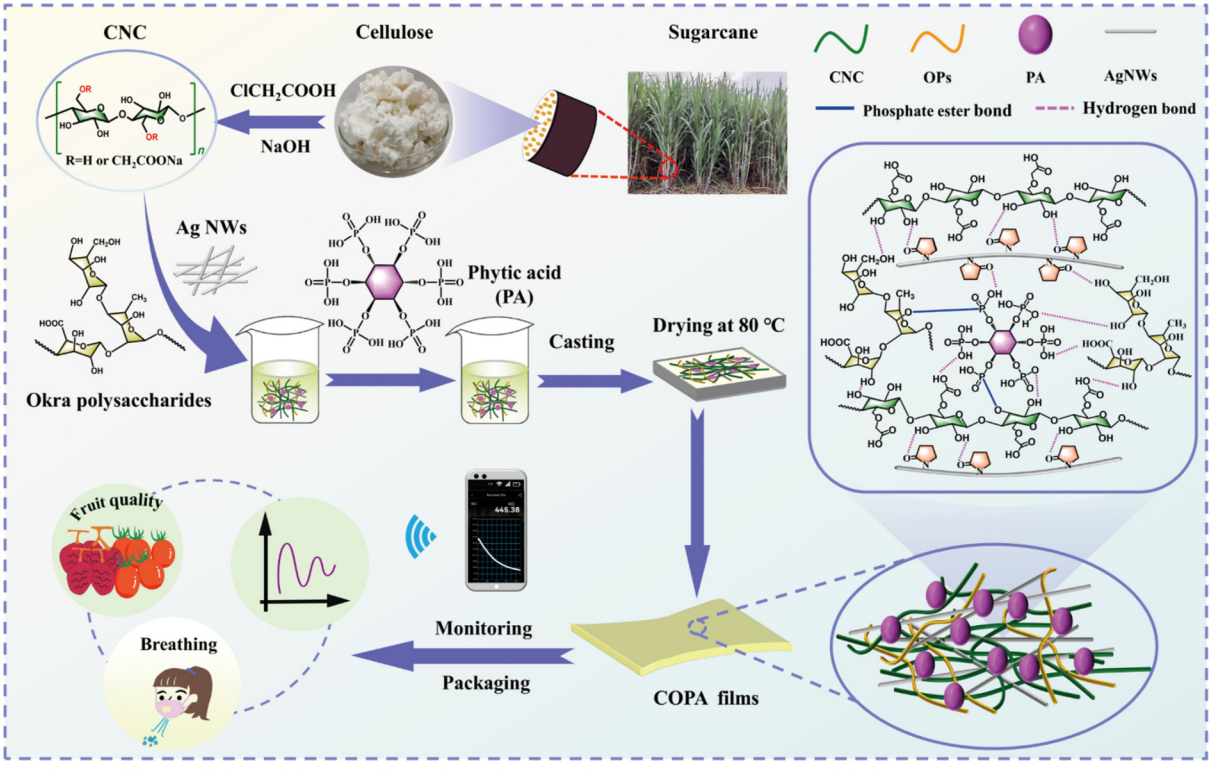

Scheme 1 Schematic of the overall design of the COPA film and its application in fruit preservation, respiration and freshness monitoring.

composite. Furthermore, PA establishes a three-dimensional cross-linked network via its six phosphate groups, coordinating with Ag NWs while reinforcing CNC/OPs interfacial interactions, which is expected to improve the mechanical strength properties and water resistance of the films. Meanwhile, the introduction of Ag NWs imparts excellent antibacterial properties to the films. This synergistic integration is expected to prepare multifunctional humidity sensors for human respiration monitoring, fruit preservation, and fruit freshness monitoring.

2.2 Characterization

The average diameters and lengths of the CNC were 4.85 and 112.71 nm, respectively (Figs. 1(a)–1(c)). The average diameter and length of the Ag NWs were approximately 59.42 nm and 9.49 μm, respectively (Figs. 1(d)–1(f)). The prepared Ag NWs solutions were well dispersed, and the ultraviolet–visible (UV–vis) spectrum of the Ag NWs revealed longitudinal and transverse plasmon absorption peaks at 350 and 385 nm, respectively (Fig. 1(g)) [14]. As shown in Fig. 1(h), the X-ray diffraction (XRD) pattern of the Ag NWs exhibits diffraction peaks that correspond to the (111), (200), (220), and (311) crystal faces of face-centered cubic silver (JCPDS#04-0783) [15, 16]. These results confirm the successful synthesis of Ag NWs. Notably, the full-range XPS spectra reveal the presence of C, N, and O elements of Ag NWs, in addition to the Ag element (Fig. 1(i)). Moreover, in the C 1s high-resolution spectra of Ag NWs, three characteristic peaks can be observed at 284.6, 285.2, and 287.4 eV, which correspond to C–C, C–N, and C=O bonds respectively. These results indicate that the surface of the prepared Ag NWs is covered with a poly(vinylpyrrolidone) (PVP) layer [17, 18]. The presence of PVP promotes the construction of hydrogen bonding networks between Ag NWs and CNC, OPs, and PA, thus improving the environmental stability of the films [17]. In addition, the visual appearance of CNC, CNC/OPs, COP, and COPA films is uniform and smooth, and the transparency decreases slightly as the Ag NWs load increases (Fig. S1 in the Electronic Supplementary Material (ESM)). However, even the COPA-1.0 film with the highest Ag NWs loading maintained good transparency.

The scanning electron microscope (SEM) images reveal that the surfaces of CNC and CNC/OPs films were smooth and continuous without defects (Figs. 2(a) and 2(b)). With the addition of PA, the surface of COP film became slightly rougher with a texture appearance, which can be due to the crosslinking between PA, CNC and OPs (Fig. 2(c)). The incorporation of Ag NWs did not significantly change the film apparent morphology, and Ag NWs were observed on the surface (Fig. 2(d)). Cross-sectional images (Figs. 2(e)–2(h)) reveal that the CNC film has a uniform distribution of "bark" layer structures, which is beneficial to the penetration of water vapor and increases water vapor permeability (WVP) of the film. With the incorporation of OPs, Ag NWs, and PA, the cross-sectional structure becomes denser and compact, which can be attributed to the crosslinking effect between the uniformly distributed OPs, Ag NWs, PA, and CNC matrix. Furthermore, the SEM-energy dispersive X-ray spectroscopy (EDS) elemental mapping images in Figs. 2(i)–2(l) show that the C, O, P,

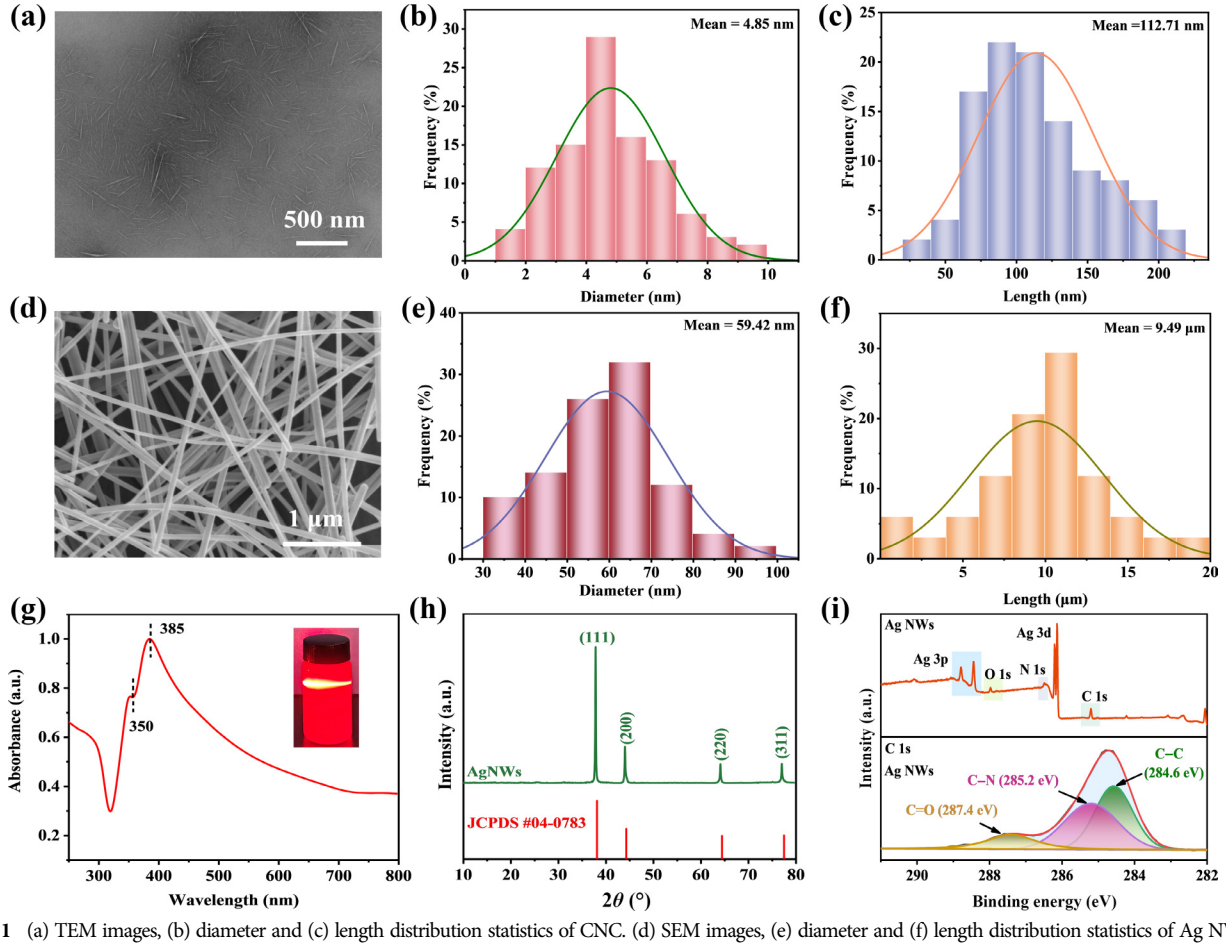

Figure 1 (a) TEM images, (b) diameter and (c) length distribution statistics of CNC. (d) SEM images, (e) diameter and (f) length distribution statistics of Ag NWs. (g) UV–vis spectrum of Ag NWs (inset: photo of Ag NWs dispersion). (h) XRD pattern, and (i) XPS survey spectrum of Ag NWs.

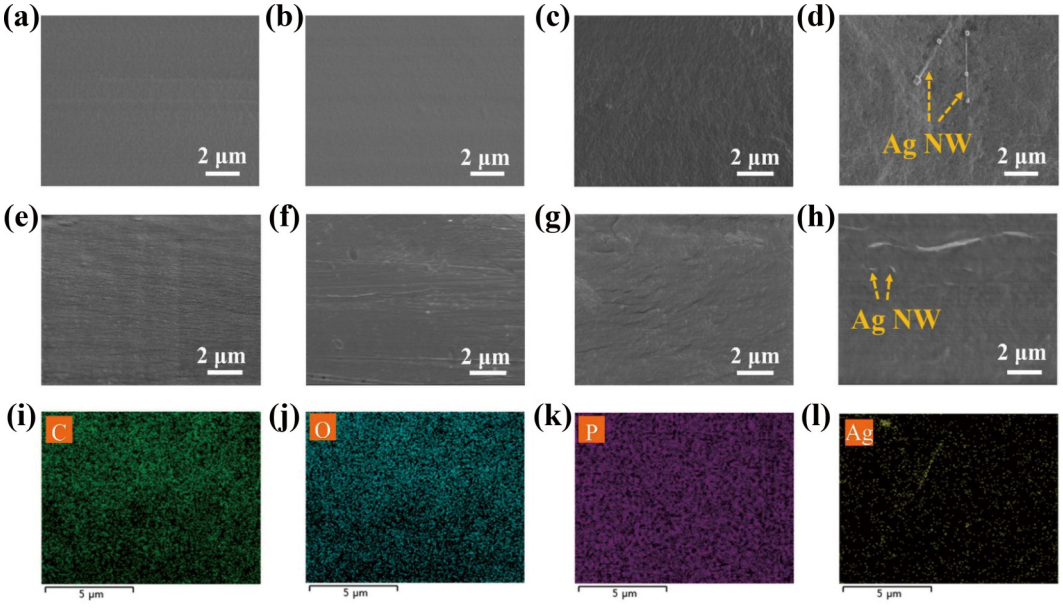

Figure 2 Surface SEM images of (a) CNC, (b) CNC/OPs, (c) COP, and (d) COPA films. Cross-section SEM images of (e) CNC, (f) CNC/OPs, (g) COP, and (h) COPA films. (i)–(l) The elemental mappings of the COPA film.

and Ag elements are uniformly distributed on the surface of the COPA films.

The Fourier transform infrared (FTIR) spectra of Ag NWs and prepared film samples are shown in Fig. 3(a). The characteristic peak of CNC film at 1061 cm^{-1} is attributed to the C–O–C stretching vibration, while the peaks at 1606 and 1418 cm^{-1} correspond to the O=C–O$^-$ stretching vibrations, indicating the presence of carboxyl groups [19]. The peak at 1630 cm^{-1} in Ag NWs is attributed to the C=O stretching vibration of PVP [20]. The simple mixing of OPs and CNC did not produce new characteristic peaks, but the stretching vibrational peaks of O=C–O$^-$ and C–O–C of CNC migrated from 1606 and 1061 to 1630 and 1057 cm^{-1}, respectively, suggesting hydrogen bonding between OPs and CNC [21]. Compared to CNC and CNC/OPs films, COP film showed absorption peaks at 1158 and 1054 cm^{-1} for P=O and P–O–C, respectively [22], indicating cross-linking of PA with the film matrix. In the FTIR spectrum of the COPA film, characteristic peaks for P=O and P–O–C were also observed. Notably, the –OH vibrational peaks (3421 cm^{-1}) showed a redshift compared to Ag NWs (3443 cm^{-1}) and COP film (3423 cm^{-1}), indicating hydrogen bonding interactions between Ag NWs and CNC, OPs, and PA. These interactions help to enhance the mechanical strength of composite films.

To further investigate the crystalline state of the materials, the XRD patterns of CNC, CNC/OPs, COP, and COPA films are surveyed. As illustrated in Fig. 3(b), all films retained the native cellulose I crystal structure with characteristic diffraction peaks located at 2θ = 14.7° (101) and 22.3° (002) [23, 24]. Notably, upon the incorporation of the OPs and PA, the diffraction peak intensity of the composite films decreased significantly, and the crystallinity index fell from 65.92% to 52.30%. This was caused by the disruption of the crystalline structure of CNC due to interactions between CNC, OPs, and PA [25, 26]. In addition, typical diffraction peaks of Ag NWs were observed at 38.0°, 44.2°, and 64.2 (2θ) for the COPA film, indicating that Ag NWs have been successfully embedded in the CNC matrix.

X-ray photoelectron spectroscopy (XPS) was employed to ascertain the chemical compositions and states of elements on the surface of materials. Compared to the CNC, CNC/OPs, and COP films, the COPA film exhibited characteristic peaks of Ag 3d orbital at 368.0 eV (Fig. 3(c)). With the addition of PA and Ag NWs, the binding energy of C=O in the C 1s region of COP and COPA exhibits a negative shift, suggesting interactions among PA, Ag NWs, CNC, and OPs (Fig. 3(d) and Figs. S2(a)–S2(c) in the ESM). Furthermore, the high-resolution C 1s and P 2p spectra of the COPA film reveal two absorption peaks at 285.2 and 133.3 eV, which correspond to C–O–P and P–O–C bonds, respectively. This demonstrates the cross-linking between PA and the composite film matrix (Figs. 3(d) and 3(e)) [22]. The narrow Ag 3d spectrum (Fig. 3(f)) exhibits two peaks of Ag $3d_{5/2}$ (368.0 eV) and Ag $3d_{3/2}$ (374.0 eV), indicating the existence of metallic silver (Ag^0) [27]. In summary, XPS analysis not only confirmed the presence of Ag NWs in the COPA film but also revealed the hydrogen and phosphate bonds cross-linking between PA and other film components, consistent with the FT-IR and XRD results.

2.3 Mechanical and thermal properties

Ideal mechanical properties are crucial for the practical application of COPA films. The CNC exhibited a tensile strength (δ_c) of 16.80 MPa and elongation at break (ε_c) of 21.66%, respectively (Figs. 3(g) and 3(h)). The δ_c and ε_c of the COP film increased to 21.76 MPa and 24.72%, respectively, which were higher than those of the CNC/OPs film (17.41 MPa and 24.38%). When the mass ratio of Ag NWs to CNC was 0.6%, the δ_c of the COPA-0.6 film reached a maximum of 26.02 MPa (54.88% higher than that of the CNC film). In conclusion, the mechanical properties of the COPA-0.6 film are significantly enhanced compared with CNC film, meeting the mechanical properties requirements for humidity sensing. Additionally, the thermal stability properties of CNC, CNC/OPs, COP, and COPA films were analyzed, and the results are shown in Fig. 3(i), Fig. S2(d) and Table S1 in the ESM. With the addition of OPs, PA, and Ag NWs, the T_{max} of the CNC/OPs, COP, and COPA films shift towards the high-temperature region, indicating enhanced thermal stability of the film.

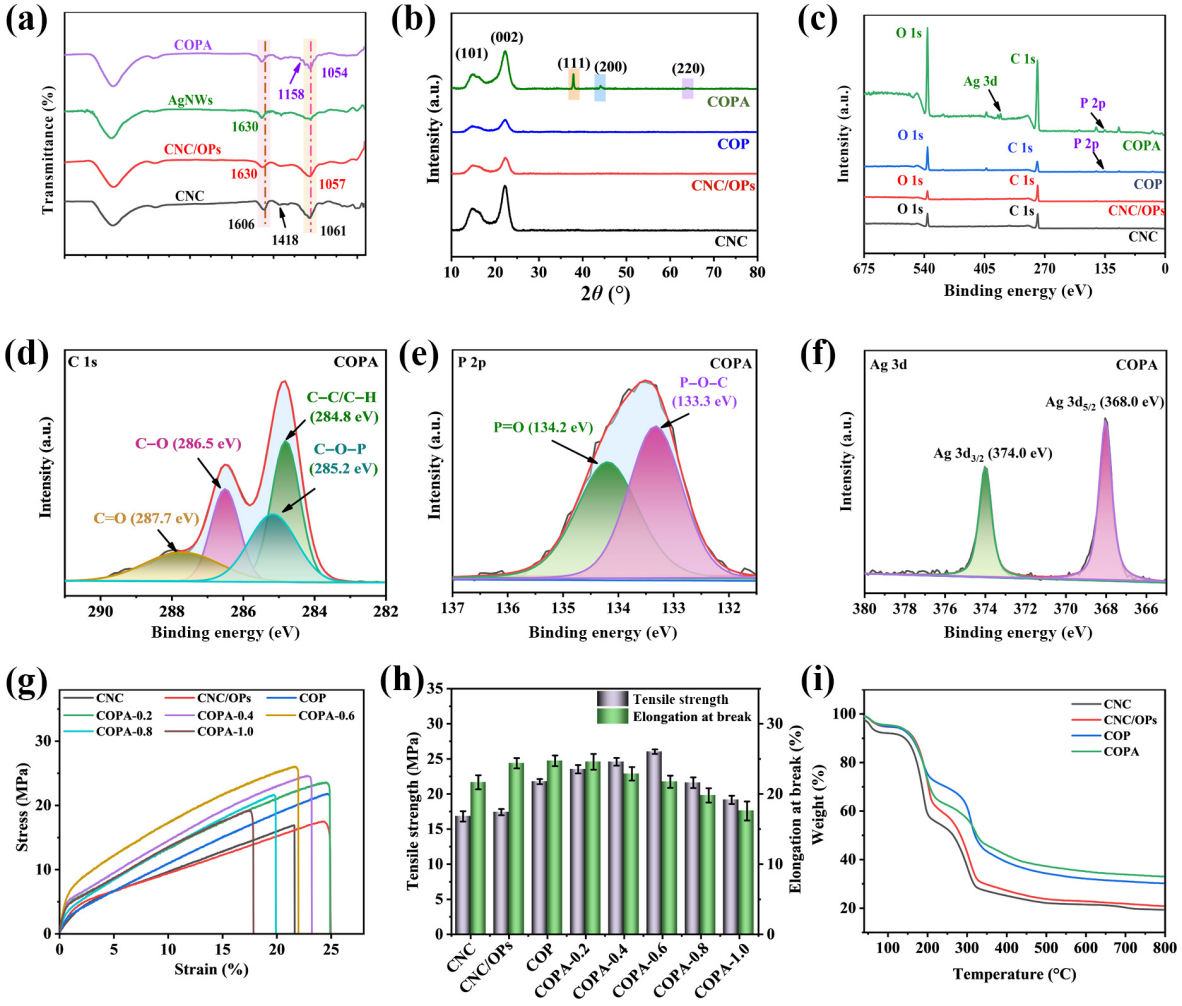

Figure 3 (a) FTIR spectra of different materials. (b) XRD and (c) XPS full spectra of CNC, CNC/OPs, COP, and COPA films. (d) C 1s, (e) P 2p, and (f) Ag 3d XPS spectra of COPA film. (g) Stress–strain curves and (h) tensile strength and elongation at break of prepared films. (i) TGA curves of CNC, CNC/OPs, COP, and COPA films.

2.4 Water resistance and water vapor barrier properties

In consideration of the importance of water resistance for film moisture sensing and packaging applications, water immersion test, film moisture content (MC), water solubility (WS), and swelling degree (SD) were used to evaluate the stability and water resistance of the films. As shown in Fig. S3 in the ESM, due to the strong hydrophilicity of CNC, the CNC films rapidly absorbed water upon immersion, leading to swelling and eventual disintegration within 10 h. In contrast, CNC/OPs films demonstrated a 4 h delay in disintegration compared to pure CNC films. This enhanced stability can be attributed to the hydrogen bonding interactions between the molecular chains of OPs and CNC. Such interactions contribute to increased film densification and a reduced disintegration rate. Notably, COP and COPA films exhibit significantly superior water resistance, retaining their structural integrity in water for up to 40 days without disintegration, outperforming both CNC and CNC/OPs films. As depicted in Fig. 4(a), the CNC film exhibits the highest MC of 19.26%, while the COP film shows the lowest MC at 11.99%. With an increase in Ag NWs loading from 0 to 1.0%, the MC of the films rises from 11.99% to 14.81%. This increase can be attributed to the incorporation of Ag NWs, which introduce additional hydrophilic groups into the matrix. Notably, films with high MC tend to promote microbial growth in practical applications. Since both CNC and OPs are strongly hydrophilic polysaccharides, CNC and CNC/OPs films are completely soluble in water, and thus their WS and SD cannot be measured. The WS and SD of COPA films decreased first and then increased with the increase of Ag NWs loading, and the WS and SD of the COPA-0.6 film were the lowest, which were 44.95% and 7.44%, respectively (Fig. 4(b)). This can be attributed to the formation of hydrogen bonds and phosphate ester bonds between CNC, OPs, and PA to reduce the number of free hydrophilic groups on the film surface, which reduces the sensitivity of the films to water.

In addition, the wettability of the film surface was further assessed through water contact angle (WCA) measurements, as illustrated in Fig. S4 in the ESM. CNC exhibits high hydrophilicity, with a WCA of 57.84°, owing to the abundance of hydrophilic groups. Upon incorporating OPs and PA, the WCA of CNC/OPs and COP films increased slightly to 62.47° and 82.69°, respectively. This can be attributed to the formation of hydrogen and hydrophobic ester bonds between OPs, PA, and CNC, improving the densification of the films and reducing the number of free hydrophilic groups on the surface, thereby decreasing the sensitivity of the films to water. It is worth noting that the addition of Ag NWs

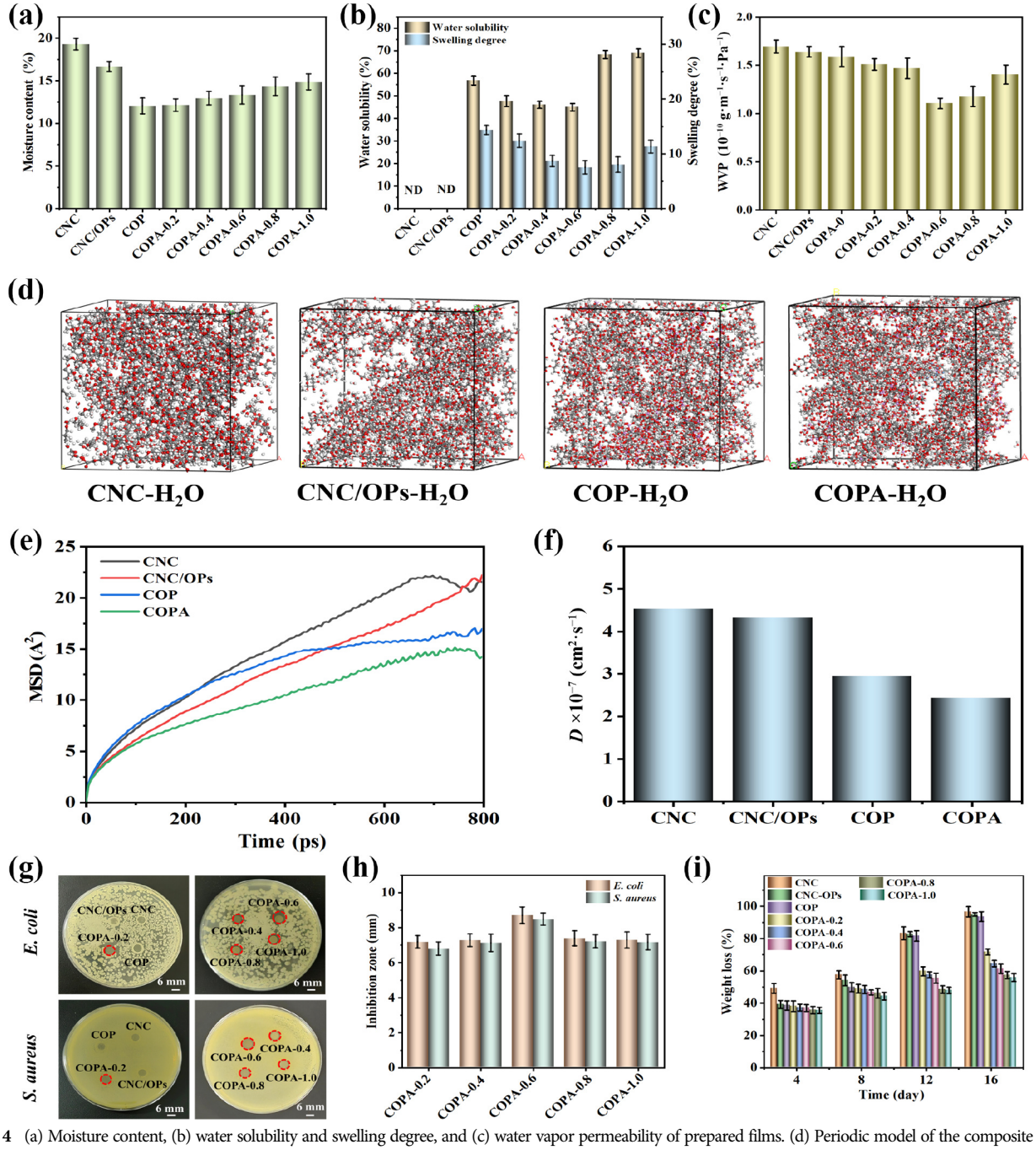

Figure 4 (a) Moisture content, (b) water solubility and swelling degree, and (c) water vapor permeability of prepared films. (d) Periodic model of the composite system containing H_2O molecules. (e) MSD and (f) diffusion coefficients (D) of water molecules in different film systems. (g) Photographs of the antimicrobial effect and (h) inhibition zones of prepared films against *E. coli* and *S. aureus*. (i) Weight loss of prepared films buried in soil.

increases the wettability of the film, which can be related to the coverage of hydrophilic PVP on the surface of Ag NWs [28, 29].

The water vapor barrier capacity of the film significantly influences both the wearing comfort of flexible sensors and the postharvest shelf-life extension of agricultural products. The WVP was measured to evaluate the barrier properties of COPA films (Fig. 4(c)). Notably, materials demonstrating lower WVP values exhibit enhanced barrier efficacy against moisture transmission, which fundamentally determines their ability to regulate humidity exchange in packaged perishables. This regulation of humidity is a critical mechanism for maintaining freshness and delaying deterioration. Specifically, the CNC film exhibits the highest moisture permeability of 1.69×10^{-10} g·m^{-1}·s^{-1}·Pa^{-1}, and the addition of OPs and PA slightly decreases the WVP of CNC/OPs and COP films to 1.64×10^{-10} and 1.59×10^{-10} g·m^{-1}·s^{-1}·Pa^{-1}, respectively. With the addition of Ag NWs, the WVP of COPA films initially decreases and then increases as the Ag NWs loading rises. The WVP of COPA-0.6 film reaches as low as 1.10×10^{-10} g·m^{-1}·s^{-1}·Pa^{-1}, which is 34.91% lower than the CNC film. This may be attributed to the spatial blocking effect of rigid Ag NWs and the interaction between Ag NWs and the matrix molecules of the composite film to form a denser structure, which hinders the diffusion of water vapor [30]. Overall, the COPA-0.6 film exhibited a lower WVP than other reported biopolymer-based films (Table S2 in the ESM).

To investigate the diffusion mechanism of H_2O molecules in CNC, CNC/OPs, COP, and COPA composite systems, molecular dynamics (MD) simulations were conducted using Materials Studio 2020 to calculate mean square displacement (MSD) and diffusion coefficients (D). As illustrated in Figs. 4(d)–4(f), the diffusion coefficients of H_2O molecules in the COP and COPA systems decreased significantly, while the CNC/OPs system shows a slight reduction in diffusion coefficients compared to the CNC system. Notably, the COPA system exhibits the lowest diffusion coefficients of 2.42×10^{-7} $cm^2 \cdot s^{-1}$. The simulation results are consistent with the experimental analysis, confirming that the synergistic effect of PA and Ag NWs effectively hinders the diffusion of water molecules.

2.5 Antibacterial and biodegradable properties

The development of sensor materials with antibacterial activity can effectively inhibit the growth of bacteria on the surface of humidity sensors, reduce the risk of infection, and extend their service life. *Escherichia coli* (*E. coli*) and *Staphylococcus aureus* (*S. aureus*) were selected as the test strains to evaluate the antibacterial effect of the prepared films by the inhibition zone method. As shown in Figs. 4(g) and 4(h), films without Ag NWs (CNC CNC/OPs, and COP) exhibited no detectable inhibitory effect against either bacterial strain. In contrast, films incorporating Ag NWs exhibited significant inhibition zones. Notably, the COPA-0.6 film showed the best inhibition effect, with inhibition zones up to 8.69 mm (*E. coli*) and 8.47 mm (*S. aureus*) in diameter. The good bacteriostatic ability of COPA films can be attributed to the presence of Ag NWs, which inactivate proteins by releasing silver ions that bind to the sulfhydryl group (–SH) of bacterial proteases, thus achieving antibacterial activity [20, 31]. Overall, the COPA films exhibited desirable antimicrobial capabilities, demonstrating promising applications in flexible smart sensors. Moreover, CNC and CNC/OPs films were significantly degraded after 8 days (Fig. 4(i) and Fig. S5 in the ESM). On the 16th day, the weight loss rate of the films without Ag NWs exceeded 93%, while those loaded with 0.2%, 0.4%, 0.6%, 0.8%, and 1.0% Ag NWs showed degradation rates above 50%, specifically 71.70%, 64.55%, 61.33%, 57.45%, and 55.88%, respectively. These results indicate that the as-prepared COPA films exhibit excellent biodegradability.

2.6 Humidity sensing response

Due to its excellent mechanical, water-resistant, and antimicrobial properties, COPA-0.6 film was selected for subsequent studies. Additionally, given the good sensitivity of CNC, OPs, PA, and Ag NWs to water molecules, the COPA-0.6 film was constructed as a humidity sensor, and its humidity response performance was investigated. The sensor exhibited excellent reproducibility, with minimal fluctuation in the response value ($\Delta R/R_0$) over five cycles at different RH levels (35%, 55%, 75%, and 98% RH) (Fig. 5(a)). The response curves for the humidification and dehumidification phases were symmetrically distributed as the COPA-0.6 humidity sensor cycled between 35%–98%–35% RH, demonstrating good reliability (Fig. 5(b)). The humidity hysteresis curve of the COPA-0.6 sensor (Fig. 5(c)) reveals the largest $\Delta R/R_0$ deviation at 43% RH, with a maximum hysteresis error of 1.24%, which is lower than that of many reported humidity sensors (Table S3 in the ESM). Notably, the COPA-0.6 sensor response values varied linearly with relative humidity in the 35%–98% RH range, with R^2 = 0.994 (Fig. 5(d)). Moreover, the response resistance of the COPA-0.6 sensor showed only minor fluctuation after 32 days of environmental exposure, demonstrating its excellent environmental durability (Fig. 5(e)).

The humidity sensing mechanism of COPA-0.6 film is shown in Fig. 5(f). Owing to the profusion of hydrophilic functional groups on the surface, the COPA-0.6 film exhibits an enhanced affinity for capturing water molecules from the environment. At low RH, the water molecules adsorbed on the surface of the film can only form a

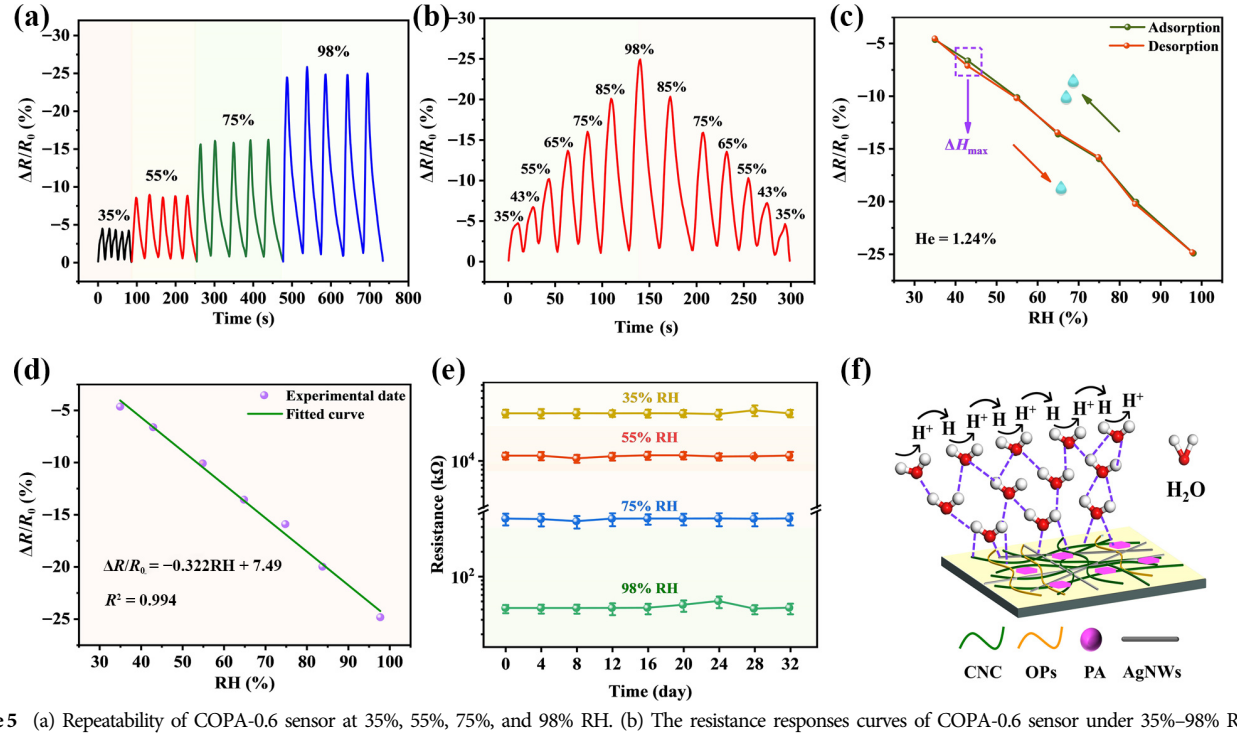

Figure 5 (a) Repeatability of COPA-0.6 sensor at 35%, 55%, 75%, and 98% RH. (b) The resistance responses curves of COPA-0.6 sensor under 35%–98% RH. (c) Hysteresis curve of COPA-0.6 sensor. (d) Linearity of COPA-0.6 sensor. (e) Durability of COPA-0.6 sensor curve. (f) Moisture-sensitive mechanism of the COPA-0.6 sensor.

single layer or a few layers of discontinuous water layer, and the proton/ion movement is difficult, resulting in high resistance. As RH increases, the highly hydrophilic COPA-0.6 film absorbs more water molecules and forms a continuous water layer. The dissociated H_3O^+ undergoes proton hopping through the Grotthus chain reaction ($H_2O + H_3O^+ = H_3O^+ + H_2O$) to promote charge transfer, thereby reducing resistance. With further increase in %RH, the adsorbed water acts as a plasticizer and the mobility of H_3O^+ increases, thus further reducing the resistance [32–34]. In addition, the phosphate group of PA can release a large number of ions in the presence of moisture, which further enhances the ionic conductivity of COPA-0.6 film and improves the humidity response performance of COPA-0.6 film [35, 36].

3 Application demonstrations

3.1 Dynamic monitoring of litchi freshness

It is well known that weight loss is a key indicator for evaluating the freshness of fruits [8, 37, 38]. During storage, a large amount of water is gradually released into the surrounding environment due to transpiration and respiration of fruit, which not only leads to severe dehydration but also promotes the growth of microorganisms, thus reducing the quality of the fruit. Therefore, the freshness of fruits can be intelligently monitored and predicted by real-time monitoring of the output resistance change of the COPA-0.6 humidity sensor in the packaging microenvironment. Based on the good water vapor barrier properties and humidity sensitivity of COPA-0.6 film, and to better validate the feasibility of COPA-0.6 humidity sensor for freshness sensing, litchi was selected as the monitoring subject for the freshness dynamic monitoring experiment. The quality change of litchi inside the box was also observed and recorded, and the constructed monitoring system is shown in Fig. S6 in the ESM. During 0–24 h, the $\Delta R/R_0$ decreased sharply (Fig. 6(a), illustration), and the weight loss rate of litchi increased significantly (Fig. 6(b)). This indicates that the respiration and transpiration of litchi in the box were intense, leading to a rapid rise in ambient humidity and a corresponding increase in the response signal intensity. Between 72–216 h, the weight loss rate of litchi increased slowly, indicating a gradual decrease in freshness. During this period, the humidity inside the box remained relatively stable, and the signals from the COPA-0.6 sensor leveled off (Figs. 6(a)–6(c)). In addition, at the beginning of storage, the initial relative humidity inside the packing box was low (66% RH), resulting in high sensor resistance (0.9691 MΩ), an unlit light-emitting device (LED) (Fig. S7 in the ESM). With prolonged storage duration, the relative humidity increased, and the brightness of the LEDs gradually intensified. Therefore, the humidity of the packaging environment can be intuitively assessed by observing the brightness of the LED lamp, enabling further assessment and prediction of the quality of the packaged fruits.

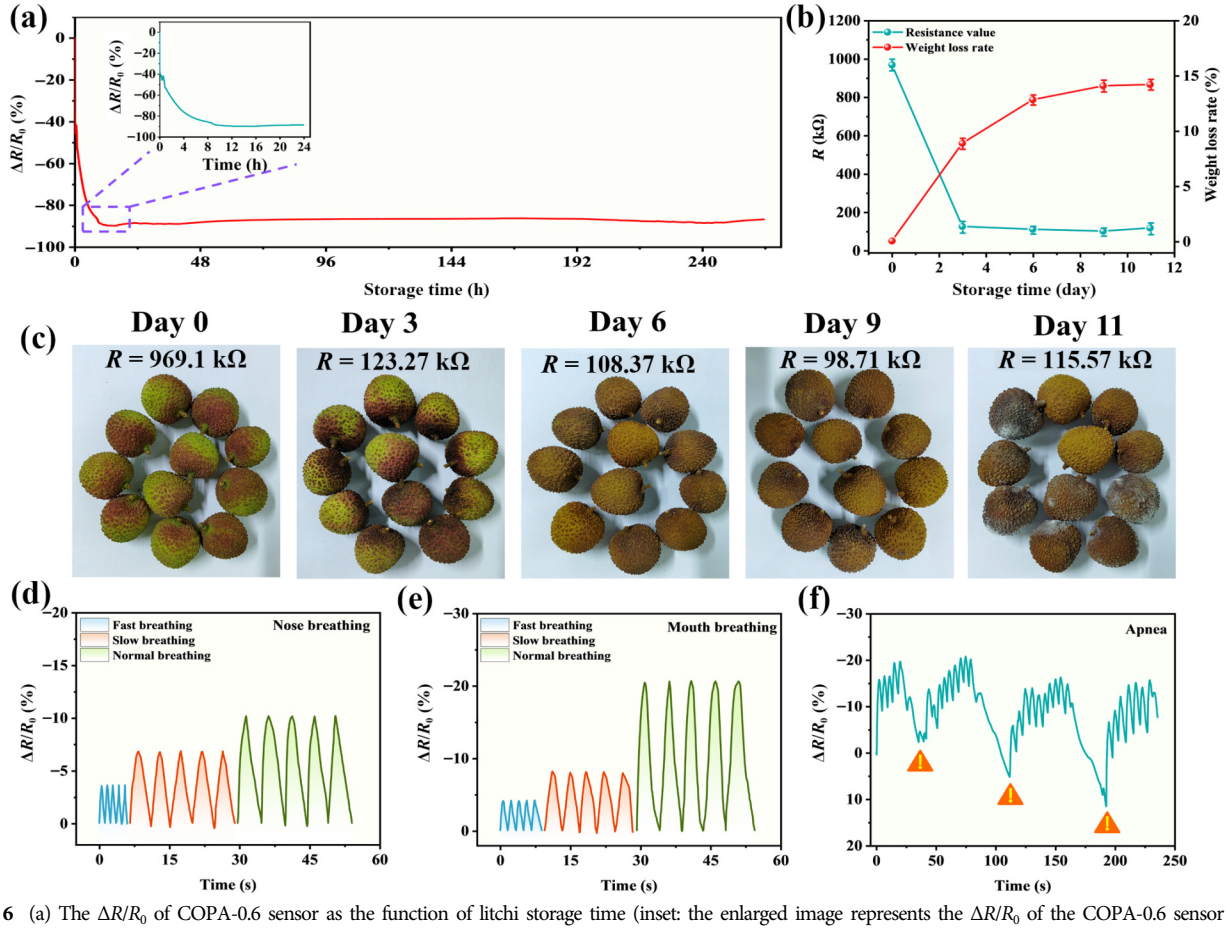

Figure 6 (a) The $\Delta R/R_0$ of COPA-0.6 sensor as the function of litchi storage time (inset: the enlarged image represents the $\Delta R/R_0$ of the COPA-0.6 sensor during 0–24 h). (b) Relationship between the weight loss rate of litchi and the storage time and the resistance of COPA-0.6 sensor. (c) Change of resistance and appearance of litchi under different storage times. Response curves of the COPA-0.6 sensor at different breathing rates through (d) nose and (e) mouth. (f) Response curve of the COPA-0.6 sensor for apnea syndrome.

3.2 Potential application in human respiratory monitoring

Considering the excellent humidity sensitivity and antibacterial properties of the COPA-0.6 film, its potential application in human respiratory monitoring was explored (Figs. 6(d)–6(f) and Movie S1 in the ESM). Based on the moisture sensitivity of the COPA-0.6 film, the resistance of the sensor decreases upon contact with water molecules in exhaled gas from the nose (Fig. 6(d)) or mouth (Fig. 6(e)) and then increases with inspiratory resistance. When apnea occurs, the response signal decreases significantly due to a sudden drop in the relative humidity of the test environment (Fig. 6(f)). Upon resuming breathing, the response signal begins to rise again. These results indicate that the COPA-0.6 sensor can judge the respiratory status of the human body according to the frequency, amplitude, and shape of the response signal, and has great potential in the field of respiratory health monitoring.

3.3 Fruit preservation applications

The preservation efficacy of commercial PE, CNC, CNC/OPs, COP, and COPA-0.6 films on fruits was comprehensively analyzed using climacteric fruits (cherry tomato) and non-climacteric (litchi) fruits as examples, with a control group. As shown in Fig. 7(a), the litchi epidermis packaged with PE film showed mold spots on the 7th day, and the litchi in the control group and the CNC group also showed mold spots on the 15th day. In contrast, no mold spots were found on the litchi epidermis packaged with CNC/OPs, COP, and COPA-0.6 films during storage, and the pulp of litchi packaged with COPA-0.6 film was fuller and fresher. Cherry tomatoes in all treatment groups maintained a good appearance on the 7th day, but cherry tomatoes in the control, PE, CNC, and CNC/OPs treatment groups rotted and mildewed on the 11th day. Thanks to the good gas barrier properties and antibacterial properties of COPA-0.6 film, cherry tomatoes packed in COPA-0.6 remained fresh until the 15th day (Fig. 7(b)). Key quality indicators such as weight loss, soluble solids (SS) content, and pH were monitored to further evaluate the preservation effect of COPA-0.6 film. The weight loss rates of litchi and cherry tomato in the control group at the end of the storage period were 20.12% and 13.04%, respectively. On the contrary, the weight loss rates of litchi and cherry tomato in COPA-0.6 film were

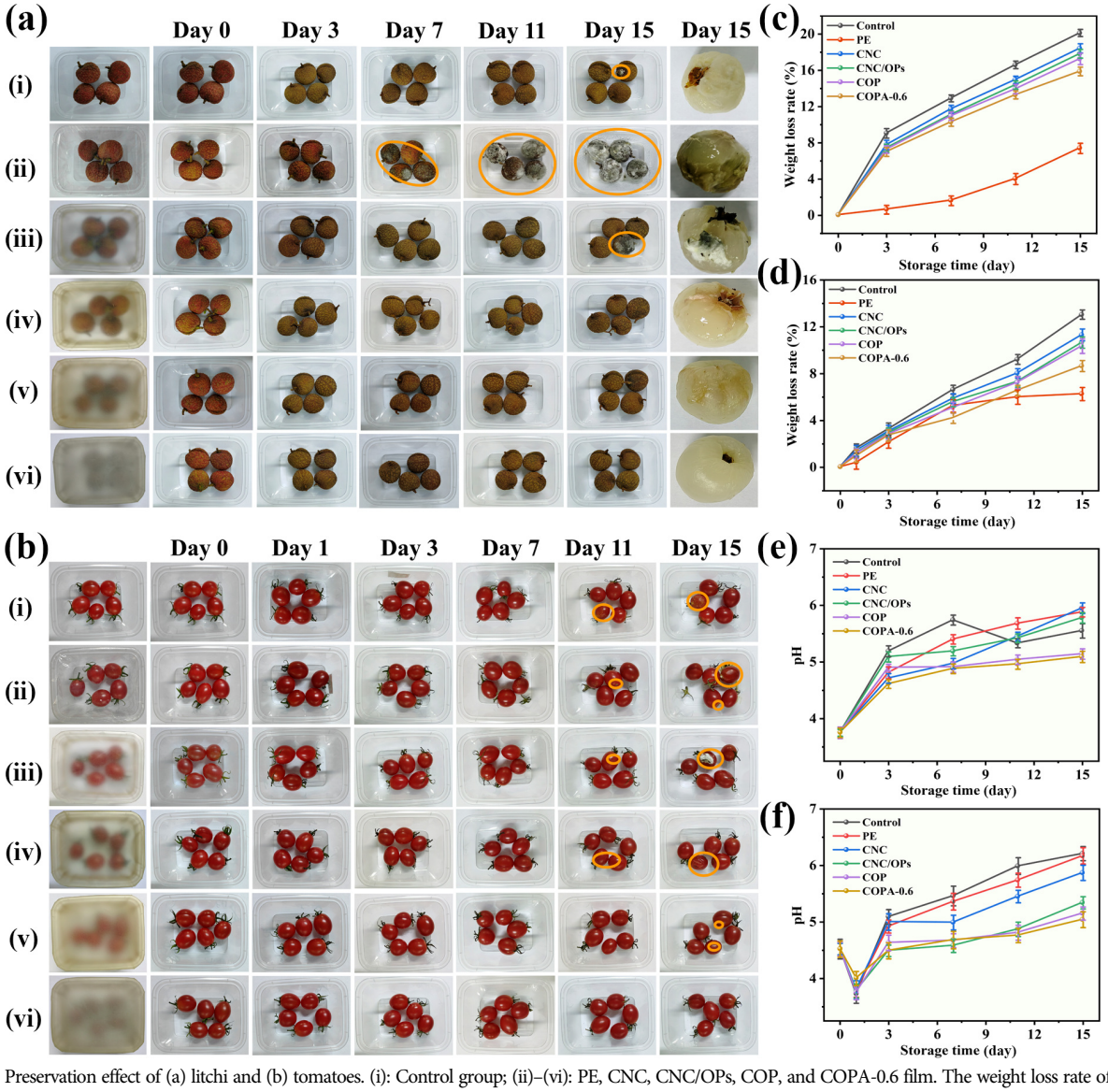

Figure 7 Preservation effect of (a) litchi and (b) tomatoes. (i): Control group; (ii)–(vi): PE, CNC, CNC/OPs, COP, and COPA-0.6 film. The weight loss rate of (c) litchi and (d) tomatoes. The pH of (e) litchi and (f) tomatoes.

significantly reduced to only 15.87% and 8.65%, respectively (Figs. 7(c) and 7(d)). This indicates that the COPA-0.6 film retarded the respiration intensity of the tested fruits to a certain degree and reduced the water loss in the fruits. Notably, due to the extremely low water vapor permeability (0.07×10^{-10}–0.27×10^{-10} g·m^{-1}·s^{-1}·Pa^{-1}) and hygroscopicity of PE film [39–41], water vapor released by the respiration of litchi and cherry tomatoes accumulated on the inner surface of the PE film (Fig. S8 in the ESM). This resulted in the lowest weight loss for wrapped litchi and cherry tomatoes (6.25% and 7.39%, respectively). As shown in Figs. 7(e) and 7(f), the pH of litchi and cherry tomatoes wrapped in COPA-0.6 film increased most slowly during storage. This indicates that the film can effectively slow down the metabolic rate of litchi and cherry tomatoes, reducing the consumption of organic acids. In addition, as illustrated in Figs. S9(a) and S9(b) in the ESM, the SS content of the fruits in all treatment groups initially increased and then decreased over time. The COPA-0.6 film group delayed the point at which SS content decreased and had a higher SS content than the other treatment groups on the 15th day. This further confirms the excellent freshness preservation properties of the COPA-0.6 film. Noteworthily, specific microbiological analyses revealed that the surfaces of litchi and tomatoes packaged with PE film were colonized by bacteria and fungi. In contrast, samples coated with COPA-0.6 film showed no visible microbial colonies, demonstrating superior antimicrobial efficacy (Figs. S10(a) and S10(b) in the ESM).

4 Conclusions

In conclusion, a flexible, degradable, multifunctional COPA composite film with high gas barrier ability, satisfactory mechanical properties, water resistance, antimicrobial properties, and humidity responsiveness was successfully prepared by the solution casting method in this study. The corresponding COPA humidity sensor has a wide detection range (35%–98% RH), high linearity (R^2 = 0.994), low hysteresis (1.24%), and long-term stability of 32 days. Thanks to its excellent humidity sensing ability, the COPA wearable humidity sensor can monitor the freshness of packaged fruit in real time and provide an early warning by connecting to smartphones and an LED bulb. Meanwhile, the COPA humidity sensor can effectively prolong the shelf life of litchi and cherry tomatoes due to the good water vapor barrier and antibacterial properties of the COPA film. This work proposes a groundbreaking method for the use of sustainable moisture-sensitive materials for fruit preservation and *in situ* non-destructive fruit freshness monitoring.

5 Experimental

5.1 Materials

SCB was supplied by Xiaopingyang Sugar Industry Co., Ltd. (Laibin, Guangxi, China). Okra was purchased from a local market (Guilin, Guangxi, China). PA (70 wt.% in H_2O), $AgNO_3$, and PVP (M_W = 1000–1,300,000) were supplied by Shanghai McLean Biochemical Technology Co. *Escherichia coli* CMCC (B) 44102 and *Staphylococcus aureus* (ATCC 6538) were purchased from Ningbo Mingzhou Biotechnology Co., Ltd.

5.2 Preparation of CNC from SCB

CNC was synthesized according to our previous reports [42]. Clean, dry SCB was ground and sieved through a 100-mesh screen. The residue was treated with 5% (w/v) NaOH and 1% (w/v) CH_3COOH solution, followed by repeated washing and drying to obtain bleached sugarcane bagasse fiber (SBF). The bleached SBF was then hydrolyzed with 5 wt.% HNO_3 and 25 wt.% CH_3COOH aqueous solution at 80 °C for 2 h, washed to neutrality, and dried. Next, the dried cellulose (24 g), 100 mL of 10 wt.% NaOH, 12 g of $CH_2ClCOOH$, and 300 mL of anhydrous ethanol solution were reacted at 75 °C for 3 h. The crude product was neutralized with 10% acetic acid and washed to pH neutrality and homogenized at high-speed shear for 2 h to obtain CNC transparent gel [43]. The gel was concentrated to 1% for further use.

5.3 Preparation of OPs

Fresh okra pulp was cut into pieces and dried in an oven at 70 °C for 6 h, then ground and sieved through a 100-mesh screen to obtain a powder. The powder (5.0 g) was mixed with 300 mL of distilled water and stirred at 80 °C for 2 h. After cooling, the solution was filtered and centrifuged. The supernatant was precipitated by 3× volume of anhydrous ethanol for 12 h, followed by centrifugation and dried to obtain OPs. The molecular weight (M_W) of the OPs was approximately 68,672 g·mol^{-1}.

5.4 Synthesis of Ag NWs

Ag NWs were synthesized via a polyol method [44]. Briefly, PVP (1.0 g) and 70 mL ethylene glycol (EG) were added to a flask and stirred at 175 °C for 30 min. Then, NaCl (0.4 M) and $AgNO_3$ (0.4 M) were added sequentially and stirred for 10 min. Next, $AgNO_3$ solution (0.5 g $AgNO_3$ in 25 mL EG) was slowly added under stirring. The product was centrifuged, washed repeatedly with deionized water, and redispersed in anhydrous ethanol to a concentration of 1.0 wt.% for further use.

5.5 Preparation of COPA films

0.1 g of OPs was added to a 1.0 wt.% CNC aqueous dispersion and stirred at 80 °C for 0.5 h. Ag NWs solutions were then added and stirred for 30 min, followed by the addition of 0.1 g of PA and continued reaction for 2 h. After degassing, the film-forming solution was decanted into a polytetrafluoroethylene mold and dried at 80 °C for 10 h to obtain COPA composite films. According to the mass ratio of Ag NWs to CNC, the composite films were labeled COPA-x (x = 0, 0.2, 0.4, 0.6, 0.8, and 1.0), respectively (Table S4 in the ESM).

5.6 Characterization

The morphology and microstructures of CNC, Ag NWs, and film samples were observed via transmission electron microscopy (TEM; JEM2100Plus, JEOL, Japan) and SEM (S4800 JEOL, Japan), respectively. The absorption spectra of the samples were obtained using FTIR (Nicolet Nexus 470, USA). The internal structure of the Ag NWs and film samples was investigated by XRD (X-Pert PRO, PANalytical B. V., Netherlands). X-ray photoelectron spectroscopy (ESCALAB 250 Xi, Thermo Scientific, USA) was employed to examine the functional groups distribution of samples, and UV–vis spectrophotometry (UV–vis; Lambda 950, UK) was employed to examine the UV–vis absorption spectra of Ag NWs suspension. Thermogravimetry of film samples ranging from 30–800 °C was performed under N_2 atmosphere by thermogravimetry (TGA; Q500, TA Instruments, USA) at a ramp rate of 10 °C·min^{-1}. The tensile stress-tests of film samples were measured using a universal testing machine (SUNS UTM14483, China). A contact goniometer

(DSA100, Kruss Scientific, Germany) was used to measure the hydrophilicity of the samples.

5.7 Water resistance

In consideration of the importance of water resistance for film moisture sensing and packaging applications, water immersion test, MC, WS, and SD were used to evaluate the stability and water resistance of the films. Briefly, a 20 mm × 20 mm sample (m_0) was dried at 80 °C to constant weight (m_1) and immersed in deionized water at room temperature for 1 day. After removal, excess water on its surface was sucked and weighed (m_2), finally dried again to constant weight (m_3). The MC, WS, and SD of the samples were calculated using Eqs. (1)–(3) [30]

$$\mathrm{MC}\,(\%) = \left(\frac{m_0 - m_1}{m_0}\right) \times 100 \quad (1)$$

$$\mathrm{WS}\,(\%) = \left(\frac{m_1 - m_3}{m_1}\right) \times 100 \quad (2)$$

$$\mathrm{SD}\,(\%) = \left(\frac{m_2 - m_1}{m_1}\right) \times 100 \quad (3)$$

5.8 Water vapor permeability of films

The WVP of the films was determined by measuring the weight change of a dried calcium chloride-filled glass bottle covered by film samples. These measurements were taken at regular intervals over a 48-hour period. The WVP was calculated using Eq. (4) [45]

$$\mathrm{WVP} = \frac{(\Delta m \times d)}{(A \times t \times P)} \quad (4)$$

where Δm (g) is the weight change of the glass bottle before and after the test, d (m) is the thickness of the films, A (m^2) is the permeation area, t (s) is the test duration, and P (Pa) is the water vapor pressure difference between the two sides of the film.

5.9 Antibacterial activity assay

E. coli (CMCC44102) and *S. aureus* (ATCC 33594) were used as test strains, and the antibacterial effect of the films was assessed by the inhibition zone. Briefly, the circular films (diameter = 0.5 cm) were placed on the culture medium that was already spread with bacterial dispersion (100 μL, 1.0×10^5 CFU·mL^{-1}). Following a 24 h incubation at 37 °C, the diameter of the inhibition zone was measured.

5.10 Biodegradability properties

Film samples (30 mm × 30 mm) were buried in natural soil at a depth of 5–8 cm, and the degradability of the films was observed and recorded every 4 days.

5.11 Humidity sensing test

Different RH levels were established using saturated salt solution: 33.28 wt.% NaOH (35% RH), K_2CO_3 (43% RH), 26.42 wt.% NaOH (55% RH), 22.80 wt.% NaOH (65% RH), NaCl (75% RH), KCl (85% RH), and saturated K_2SO_4 (98% RH). In addition, the dry $CaCl_2$ provides a dry environment (0% RH). The RH values were calibrated by a commercial hygrometer before testing. The as-prepared film（20 mm × 10 mm × 0.08 mm） was placed into different RH environments and connected to a digital multimeter to collect resistance signals. The experiments were conducted at 25 °C. The relative resistance change ($\Delta R/R_0$) can be expressed as $\Delta R/R_0 = (R - R_0)/R_0$, where R_0 and R represent the resistance before and after test, respectively. The hysteresis error (He) was defined as $\mathrm{He} = (\pm\Delta H_{max})/(2Y) \times 100\%$, where ΔH_{max} is the maximum difference in response between forward and reverse processes and Y is the full-scale output [46].

5.12 Fruit preservation and intelligent monitoring

Fresh litchi and tomatoes of comparable size, ripeness, and undamaged appearance were procured from local markets. They were then randomly divided into 6 groups and placed into plastic boxes. One group was left unwrapped while the other five groups were wrapped with PE, CNC, CNC/OPs, COP, and COPA-0.6 films, respectively. Finally, all samples were stored at 24 ± 3 °C and 60%–65% RH. The appearance, weight loss, SS content, and pH changes of the samples were observed and measured periodically. The weight loss rate was described by the following Eq. (5)

$$\text{Weight loss rate}\,(\%) = \frac{W_0 - W_t}{W_0} \times 100 \quad (5)$$

where W_0 and W_t are the initial and the real-time weight, respectively.

In addition, fresh litchi was selected as the target for the freshness monitoring verification experiment. First, 250 g of fresh, non-destructive "Feizixiao" litchi was weighed and placed into the packing box. Then, a COPA-0.6 humidity sensing film (20 mm × 1.0 mm × 0.08 mm) was connected to a multimeter and placed into the box to monitor the resistance change. The actual temperature and humidity inside the box were measured by a commercial thermo-hygrometer.

5.13 Molecular dynamics simulations

The diffusion mechanism of H_2O molecules in CNC, CNC/OPs, COP, and COPA composite films was simulated using the corresponding model systems, Materials Studio 2020 software with Forcite, Amorphous Cell modules, and a Universal force field. The degree of polymerization for both CNC and OPs was set to 10, and the number of water molecules in the crystal cell was determined using the sorption module at 298.15 K (25 °C) under a constant pressure of 100 kPa. The MSD was calculated by Eq. (6)

$$\mathrm{MSD}\,(t) = \frac{1}{N}\sum_{i=1}^{N}\left[r_i\,(t) - r_i\,(0)\right]^2 \quad (6)$$

where r_i (0) and r_i (t) are the positions of the molecule at the initial and time t, respectively. N is the equivalent number of particles.

The diffusion coefficient (D) is calculated by Einstein's method using Eq. (7) [47]

$$D = \frac{1}{6N}\lim_{t\to\infty}\frac{\mathrm{d}}{\mathrm{d}t}\sum_{i=1}^{N}\left\langle\left|r_i\,(t) - r_i\,(0)\right|\right\rangle^2 \quad (7)$$

Electronic Supplementary Material: Supplementary material (including the detailed data of digital photographs of fabricated films, XPS, DTG, water immersion test, WCA, digital photographs of degradation process, monitoring litchi freshness device diagram, time-dependent humidity and resistance, thermogravimetric analysis data, comparison of the water vapor barrier properties, humidity sensors performance, and the composition of fabricated

films) is available in the online version of this article at https://doi.org/10.26599/NR.2025.94907804.

Data availability

All data needed to support the conclusions in the paper are presented in the manuscript and the Electronic Supplementary Material. Additional data related to this paper may be requested from the corresponding author upon request.

Acknowledgments

The authors gratefully acknowledge financial support provided by the National Natural Science Foundation of China (Nos. 52363014 and 22405179), the Science and Technology Project of Guangxi (GK AB23026136), and the Open Fund Funding of Key Laboratory of New Processing Technology for Nonferrous Metal & Materials, Ministry of Education/Guangxi Key Laboratory of Optical and Electronic Materials and Devics (22AA-7).

Declaration of competing interest

All the contributing authors report no conflict of interests in this work.

Author contribution statement

Q. Y. W.: Conceptualization, methodology, validation, formal analysis, and writing – original draft. L. D. Y., D. C. L., and Y. Y. H.: Resources, methodology, investigation. Y. L. L., R. B. S., and Z. W. L.: Data curation, methodology, investigation. W. D. Z. and Z. C. Z.: Data curation, formal analysis, and software. Y. P. D.: Methodology. S. R. L.: Writing – review and editing, project administration, and funding acquisition.All the authors have approved the final manuscript.

Use of AI statement

None.

References

[1] Liu, Z. J.; Zhang, J. K.; Cai, Y.; Wang, H.; Luo, M. J.; Li, J. Y.; Yu, H.; Meng, X. B.; Cao, Y. H. Improving seed shattering resistance in wild *O. alta* rice with mesoporous silica nanoparticle delivery systems. *Nano Lett.* **2024**, *24*, 11823–11830.

[2] Priyadarshi, R.; Uzun, S.; Rhim, J W. Edible coating using carbon quantum dots for fresh produce preservation: A review of safety perspectives. *Adv. Colloid Interface Sci.* **2024**, *331*, 103211.

[3] Cui, Y. Q.; Cheng, Y. X.; Xu, Z.; Li, B. C.; Tian, W. G.; Zhang, J. Cellulose-based transparent edible antibacterial oxygen-barrier coating for long-term fruit preservation. *Adv. Sci. (Weinh.)* **2024**, *11*, e2409560.

[4] Prasad, A.; Khan, S.; Monteiro, J. K.; Li, J. X.; Arshad, F.; Ladouceur, L.; Tian, L.; Shakeri, A.; Filipe, C. D. M.; Li, Y. F. et al. Advancing *in situ* food monitoring through a smart lab-in-a-package system demonstrated by the detection of *Salmonella* in whole chicken. *Adv. Mater.* **2023**, *35*, 2302641.

[5] Maimaiti, A.; Zhu, K.; Yan, B. Dual-mode bionic visual-olfactory co-sensory for on-site biogenic amines recognition and food freshness prediction. *Adv. Funct. Mater.* **2025**, *35*, 2412817.

[6] Wang, D. Y.; Zhang, M.; Zhu, Q. B.; Adhikari, B. Intelligent vegetable freshness monitoring system developed by integrating eco-friendly fluorescent sensor arrays with deep convolutional neural networks. *Chem. Eng. J.* **2024**, *488*, 150739.

[7] Du, J.; Jiao, C. Q.; Li, C.; Tao, Y. H.; Lu, J.; Cheng, Y.; Xia, X. D.; Tan, M. Q.; Wang, H. S. Eco-friendly and humidity-sensitive cellulosic triboelectric materials tailored by xylanase for monitoring the freshness of fruits. *Nano Energy* **2023**, *116*, 108803.

[8] Deng, P. P.; Wang, Z. H.; Li, Y. W.; Ji, S. M.; Sun, Y. F.; Deng, Q. X.; Chen, J. J.; Jiang, F. T. High strength, gas barrier and hydrophobic konjac glucomannan/glutenin films with semi-interpenetrating network for cherry tomato preservation. *Food Hydrocoll.* **2025**, *160*, 110861.

[9] Huang, L.; He, X. Y.; Hu, J. M.; Qin, C. X.; Huang, C. X.; Tang, Y.; Zhong, F. L.; Kong, X. Z.; Wei, X. Wearable sensor based on covalent organic framework humidity films for long-term monitoring of tomato physiology under abiotic stress. *ACS Nano* **2024**, *18*, 33105–33118.

[10] Wang, B.; Han, B.; Wang, K.; Cao, S. L. Air vehicle humidity sensor based on PVA film humidity sensing principle. *APL Mater.* **2024**, *12*, 071116.

[11] Li, X. Y.; Ma, Y.; Choi, C.; Ma, X. Z.; Chatterjee, S.; Lan, S. F.; Hipwell, M. C. Nanotexture shape and surface energy impact on electroadhesive human-machine interface performance. *Adv. Mater.* **2021**, *33*, 2008337.

[12] Liu, X.; Hou, C.; Liu, Y.; Chen, S. F.; Wu, Z. T.; Liang, X. C.; Tai, G. A. Borophene and BC_2N quantum dot heterostructures: Ultrasensitive humidity sensing and multifunctional applications. *J. Mater. Chem. A* **2023**, *11*, 24789–24799.

[13] Lv, Z. Y.; Zhu, S. R.; Wang, Y.; Ren, Y. Y.; Luo, M. T.; Wang, H. N.; Zhang, G. H.; Zhai, Y. B.; Zhao, S. L.; Zhou, Y. et al. Development of bio-voltage operated humidity-sensory neurons comprising self-assembled peptide memristors. *Adv. Mater.* **2024**, *36*, 2405145.

[14] Wang, L. Y.; Kong, Y. Y.; Zhang, Z. H.; Luo, G. H.; Hou, X. J.; Su, A.; Yang, X.; Wu, K. J. Streamlined synthesis of silver nanowires using multi‐objective optimization for electrically conductive composite filaments. *Adv. Funct. Mater.* **2024**, *34*, 2407999.

[15] Fang, F.; Huang, G. W.; Xiao, H. M.; Li, Y. Q.; Hu, N.; Fu, S. Y. Largely enhanced electrical conductivity of layer-structured silver nanowire/polyimide composite films by polyaniline. *Compos. Sci. Technol.* **2018**, *156*, 144–150.

[16] Hang, T. Y.; Zhou, L. J.; Xu, C. H.; Chen, Y. M.; Shen, J. H.; Zheng, J. J.; Yang, P. G.; Li, X. P.; Luo, H.; Tong, G. X. High-performance wearable bimetallic nanowire-assisted composite foams for efficient electromagnetic interference shielding, infrared stealth, and piezoresistive sensing. *Nano Res.* **2024**, *17*, 6757–6765.

[17] Lei, Z. M.; Lv, F. L.; Wang, X. R.; Li, J. Q.; Zhao, J. X.; Lyu, S. S.; Hu, Y. G.; Mo, D. C. Flexible sandwich-structured silver nanowire/exfoliated graphite platelet/aramid nanofiber composite films with excellent EMI shielding, thermal conduction and Joule heating performances. *Compos. Part A: Appl. Sci. Manuf.* **2024**, *186*, 108433.

[18] Dai, Y. H.; Sun, N.; Jiang, D. X.; Wang, Z. F.; Ding, Q.; Zhang, Z.; Liu, Y. Ultrathin and highly flexible layered silver nanowires/carboxymethyl cellulose nanofiber nanocomposite films for electromagnetic interference shielding. *Int. J. Biol. Macromol.* **2024**, *278*, 134770.

[19] Cao, Q.; Chen, J.; Wang, M.; Wang, Z. G.; Wang, W. J.; Shen, Y. Q.; Xue, Y.; Li, B.; Ma, Y. L.; Yao, Y. J. et al. Superabsorbent carboxymethyl cellulose-based hydrogel fabricated by liquid-metal-induced double crosslinking polymerisation. *Carbohydr. Polym.* **2024**, *331*, 121910.

[20] Wang, J. J.; Zhou, Q.; Wang, A.; Zhu, Z. J.; Moses, K.; Wang, T. J.; Li, P.; Huang, W. Sponge inspired flexible, antibacterial aerogel electrode with long-term high-quality electrophysiological signal recording for human-machine interface. *Adv. Funct. Mater.* **2024**, *34*, 2309704.

[21] Ormanli, E.; Bayraktar, O.; Şahar, U.; Tavman, S.; Kumcuoglu, S. Development and characterization of films based on okra polysaccharides and whey protein isolate. *J. Food Meas. Charact.* **2023**, *17*, 264–277.
[22] Zhang, Z. H.; Zhou, Z. Z.; Huang, J. C.; Wang Y. H. A flame retardant poly vinyl alcohol/graphene oxide/phytic acid composite for a quick response and ultra-long fire alarm. *J. Mater. Chem. A* **2024**, *12*, 6050–6066.
[23] Han, M. M.; Shen, W. H.; Tong, X.; Corriou, J. P. Cellulose nanofiber/MXene/AgNWs composite nanopaper with mechanical robustness for high-performance humidity sensor and smart actuator. *Sens. Actuators B: Chem.* **2024**, *406*, 135375.
[24] Tang, J. F.; Fan, X. Q.; Huang, H. Z.; Dong, X. F.; Li, X. Q.; Wang, P. R.; Yin, R.; Xie, Y. J.; Li, J.; Tan, G. et al. Biodegradable, strong, and clear wood package for plastic alternative. *Nano Res.* **2024**, *17*, 8531–8541.
[25] Kang, S. L.; Wang, H. L.; Xia, L.; Chen, M. M.; Li, L. L.; Cheng, J. F.; Li, X. J.; Jiang, S. T. Colorimetric film based on polyvinyl alcohol/okra mucilage polysaccharide incorporated with rose anthocyanins for shrimp freshness monitoring. *Carbohydr. Polym.* **2020**, *229*, 115402.
[26] Nita, L. E.; Chiriac, A. P.; Ghilan, A.; Rusu, A. G.; Tudorachi, N.; Timpu, D. Alginate enriched with phytic acid for hydrogels preparation. *Int. J. Biol. Macromol.* **2021**, *181*, 561–571.
[27] Mai, X.; Xue, B.; Zeng, L. J.; Zhang, J. X.; Xie, L. Asymmetric sandwich poly(lactic acid) composite films fabricated by one-step phase separation approach towards absorption-dominant electromagnetic interference shielding and hydrophobicity. *Chem. Eng. J.* **2024**, *499*, 156511.
[28] He, L.; Yao, Q. Y.; Xu, Y. N.; Shao, X. M.; Chen, Y.; Feng, D.; Wang, W. C. Flexible, hydrophobic, and robust composite films with sandwich structure for electromagnetic interference shielding and Joule heating. *Polymer* **2024**, *298*, 126890.
[29] Jia, L. C.; Zhang, G. Q.; Xu, L.; Sun, W. J.; Zhong, G. J.; Lei, J.; Yan, D. X.; Li, Z. M. Robustly superhydrophobic conductive textile for efficient electromagnetic interference shielding. *ACS Appl. Mater. Interfaces* **2019**, *11*, 1680–1688.
[30] Zhang, T.; Wang, H. Y.; Hu, H.; Li, W. X.; Zhang, X. D.; Zhang, X. R. Composite film based on carboxymethyl cellulose and gellan gum with honokiol-β-cyclodextrin inclusion complex: Characterization and application in strawberry preservation. *Int. J. Biol. Macromol.* **2024**, *282*, 136740.
[31] Wang, Z.; Li, S. B.; Yang, X.; Wang, H.; Xie, L. J.; Tao, Z. C.; Kong, Q. Q.; Zhang, S. C.; Jia, H.; Jiang, D. et al. Towards wearable multifunctional cellulose nanofiber/silver nanowire/graphene oxide film: Electromagnetic protection, antibacterial, and motion monitoring. *Chem. Eng. J.* **2024**, *502*, 157751.
[32] Jiang, Y.; Wu, L. B.; Chen, Q.; Li, N.; Tian, J. D. High-performance capacitive humidity sensor based on flower-like SnS_2/Ti_3C_2 MXene for respiration monitoring and non-contact sensing. *Sens. Actuators B: Chem.* **2025**, *426*, 137012.
[33] Geng, M. R.; Zhao, J. Q.; Li, J.; Liu, B. Y.; Liu, R. M.; Wang, X. J.; Song, W. L.; Shao, M. Z.; Luan, Y. H.; Li, Q. et al. Facilitating response/recovery of cellulosic humidity sensor by densificating fibril arrays. *Chem. Eng. J.* **2024**, *500*, 157221.
[34] Liu, H.; Qin, J. X.; Yang, X. G.; Lv, C. F.; Huang, W. T.; Li, F. K.; Zhang, C.; Wu, Y. R.; Dong, L.; Shan, C. X. Highly sensitive humidity sensors based on hexagonal boron nitride nanosheets for contactless sensing. *Nano Res.* **2023**, *16*, 10279–10286.
[35] Berber, M. R.; Hafez, I. H. Boosting the proton conductivity, chemical stability, and fuel cell performance of nafion membrane at high operating temperatures and low humidity levels by incorporating phytic acid. *Int. J. Hydr. Energy* **2024**, *57*, 1126–1138.
[36] Xing, R. Q.; Liu, Y.; Yan, J.; Wang, R.; Zhuang, X. P.; Yang, G. High-performance, breathable and flame-retardant moist-electric generator based on asymmetrical nanofiber membrane assembly. *J. Colloid Interface Sci.* **2024**, *671*, 205–215.
[37] Liu, Y.; Ding, Y.; Wang, C.; Luo, J.; Yao, H. H.; Zhang, H. L.; Xu, L.; Niu, J. F. High-adhesion antimicrobial composite coating incorporating quaternary chitosan and tea tree oil for enhanced preservation of fruits and vegetables. *Food Chem.* **2025**, *465*, 142007.
[38] Yu, Y. Y.; Zhou, J. J.; Chen, Q. Q.; Xie, F.; Zhang, D.; He, Z. J.; Cheng, S. Y.; Cai, J. Self-reinforced multifunctional starch nanocomposite film for litchi fruit postharvest preservation. *Chem. Eng. J.* **2024**, *486*, 150262.
[39] Yang, J.; Zhou, Z. L.; Lu, P.; Wu, M. Leaf porous structure Inspired packaging film for fruits preservation and monitoring CO_2 concentration of package. *Chem. Eng. J.* **2023**, *464*, 142660.
[40] Xie, D. H.; Huang, G. H.; Yang, M. H.; Yi, S. M.; Zheng, X. G.; Zhu, M. G.; Zhai, H. Y. Bionic modified atmosphere film Inspired by plant stomata with curcumin as controllable gas "Switches" for fruit preservation. *Chem. Eng. J.* **2024**, *500*, 156741.
[41] Lange, J.; Wyser, Y. Recent innovations in barrier technologies for plastic packaging—A review. *Packag. Technol. Sci.* **2003**, *16*, 149–158.
[42] Wei, Q. Y.; Li, D. C.; Lao, Y. F.; Xiao, S. J.; Ye, L. D.; Wang, Z.; Li, Z. W.; Lu, S. R. Multifunctional bagasse nanocellulose-based composite films reinforced by the synergy of phytic acid/tannic acid for fast-response breath monitoring sensors. *Chem. Eng. J.* **2024**, *499*, 155988.
[43] Li, X.; Xiao, S. J.; Lao, Y. F.; Li, D. C.; Wei, Q. Y.; Ye, L. D.; Lu, S. R. A nanocellulose-based flexible multilayer sensor with high sensitivity to humidity and strain response for detecting human motion and respiration. *Int. J. Biol. Macromol.* **2024**, *266*, 131004.
[44] Doganay, D.; Coskun, S.; Kaynak, C.; Unalan, H. E. Electrical, mechanical and thermal properties of aligned silver nanowire/polylactide nanocomposite films. *Compos. Part B: Eng.* **2016**, *99*, 288–296.
[45] Geng, C.; Jiang, Y. F.; Bian, H. D.; Huang, G. H. Selective gas-permeation films with nanoMOFs as gas "Switches" for mango preservation. *Chem. Eng. J.* **2024**, *481*, 148757.
[46] Zhang, Z. C.; Lu, T. Y.; Yang, D.; Lu, S. R.; Cai, R.; Tan, W. H. A high-wet-strength biofilm for readable and highly sensitive humidity sensors. *Nano Lett.* **2021**, *21*, 9030–9037.
[47] Sun, M. Y.; Lin, L.; Di, H. S.; Feng, Y. H. A study on the effects of lignocellulosic biomass components on the interactions and thermal conductivity of stearic acid: Molecular dynamics simulation. *Int. J. Heat Mass Transfer* **2025**, *244*, 126932.